From semiconductor to Fermi metal and emergent density-wave-like transition in the quasi-one-dimensional *n*-type Bi$_{19}$S$_{27}$I$_3$ under hydrostatic pressure

Shuxiang Xu [1,2] Ziyi Liu,[1,2] Pengtao Yang [1,2] Binbin Ruan,[1,2] Zhian Ren,[1,2] Jianping Sun [1,2] Yoshiya Uwatoko,[3] Bosen Wang [1,2,*] and Jinguang Cheng [1,2,†]

[1]*Beijing National Laboratory for Condensed Matter Physics and Institute of Physics, Chinese Academy of Sciences, Beijing 100190, China*
[2]*School of Physical Sciences, University of Chinese Academy of Sciences, Beijing 100190, China*
[3]*Institute for Solid State Physics, University of Tokyo, Kashiwanoha 5-1-5, Kashiwa, Chiba 277-8581, Japan*

We report on crystal growth and physical properties of the quasi-one-dimensional compound Bi$_{19}$S$_{27}$I$_3$ by combining crystal structure, electrical resistivity, magnetic properties, Seebeck coefficient, Hall coefficient as well as hydrostatic pressure effect up to 11.5 GPa. Unlike *p*-type Bi$_{19}$S$_{27}$I$_3$ crystals, the maximum size of high-quality *n*-type Bi$_{19}$S$_{27}$I$_3$ crystals can reach 2–3 mm by optimizing the chemical vapor transport method. The measurement results indicate that Bi$_{19}$S$_{27}$I$_3$ is a diamagnetic semiconductor with two thermal activation energies, a large one $E_{g1} \sim 0.81$ eV and a small one $E_{g2} \sim 0.36$ eV, a huge room-temperature Seebeck coefficient of -1000 µV/K, and improved thermoelectric power factor ~ 2.2 µW cm^{-1} K^{-2} owing to the enhanced electrical conductivity. Under pressure, Bi$_{19}$S$_{27}$I$_3$ undergoes a semiconductor-to-metal transition, and the thermal activation energy continuously decreases to almost zero near a critical pressure of 4.25 GPa. Accompanying this process, a density-wave-like transition emerges, characterized by the reversible jump observed in the temperature dependence of the resistivity. As the pressure further increases, the resistivity undergoes a crossover from a Fermi metal to a low-temperature upturn below a characteristic temperature, which decreases from 81 K at 4.5 GPa to 37 K at 11.5 GPa. The upturn in resistivity has a linear dependence on the logarithmic temperature, but does not saturate at low temperatures, which basically excludes a Kondo-like state and indicates the possibility of Anderson weak localization. High-pressure synchrotron x-ray diffraction confirms the absence of structural transition for $P < 12.05$ GPa at room temperature, supporting pressure-induced electronic transition. Our density functional theory calculation on the assumption that the Bi1 occupies an average of $\sim \frac{1}{6}$ contradicts experimental electron bands, indirectly indicating that Bi1 should be partially ordered and has many vacancies in Bi$_{19}$S$_{27}$I$_3$. Our results provide good examples for studying the mechanism of semiconductor metallization and exploring thermoelectric functional properties in low-dimensional materials.

I. INTRODUCTION

For a long time, bismuth-containing compounds have attracted widespread attention due to interesting physical phenomena and the emergence of multifunctional materials [1–15], for example, metal-insulator transition, charge order (CO), and high−T_c superconductivity (SC) in Ba$_{1-x}$(K, Pb)$_x$BiO$_3$ [3–6], topological insulator and possible topological superconducting states in Cu$_x$Bi$_2$Se$_3$ and Bi$_2$Se$_3$ under pressure [7–10], single-phase multiferroics in the helical magnetic BiFeO$_3$ [11,12], and excellent thermoelectric performance in Bi$_2$(S, Se, Te)$_3$ [1,2,13–15]. It is generally believed that these interesting properties and phenomena are closely related to strong spin-orbit coupling and the presence of 6*s* lone pair electrons of bismuthide [16–20]. At the same time, the Bi-containing compounds usually display multi-structural transitions and complex electronic states, which are simultaneously sensitive to the external stimulation and could be highly manipulated through element doping, magnetic

field, and pressure, etc. [4–10,15,19,20]. Thus, the bismuth-contained compounds provide a good platform for studying the evolution of various competitive excited states via a clean method, such as low-dimensional charge-/spin-density wave (CDW/SDW) [21–24], CO, SC [4–6], and possible topological electronic phase transitions [7–10]. These scientific achievements not only help to reveal the underlying mechanisms of functional properties but also have important significance for future experimental explorations.

The Bi$_{19}$S$_{27}$I$_3$ is a good example with a quasi-one-dimensional (Q1D) characteristic and a promising high-temperature thermoelectric material with a considerable $ZT \sim 0.04$ at 673 K [25–27]. As depicted in Fig. 1, the hexagonal Bi$_{19}$S$_{27}$I$_3$ is featured by a complexed three-dimensional (3D) network with the unique Q1D-Bi1 atom chain along the *c* axis. The Bi1 atoms occupy the vertices of a rhombic quadrilateral, and a six-coordinated radiative Bi-S infinite chain is formed around each Bi1 atom. For each chain, the atomic arrangement order is Bi1-S1-Bi2-S2-Bi3-S3. The nearest three Bi1 clusters are connected by Bi3-I bonds, which ultimately determine the network structure in the *ab* plane and the Q1D structure along the *c* axis [26,27]. These characteristics show that Bi$_{19}$S$_{27}$I$_3$ should have complex Fermi surfaces accompa-

*bswang@iphy.ac.cn
†jgcheng@iphy.ac.cn
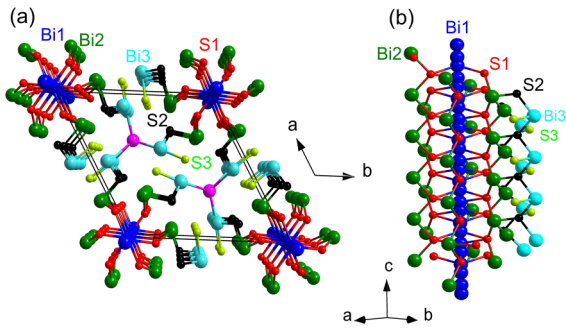
FIG. 1. Crystal structure of hexagonal $Bi_{19}S_{27}I_3$. (a) Top view of the crystal structure. The Bi1 atoms occupy the vertices of a rhombic quadrilateral, and a six-coordinated radiative Bi-S infinite chain is formed around each Bi1 atom. The Bi3-I bonds connect the Bi-S infinite chains. (b) Crystal structure viewed from the side and the quasi-one-dimensional Bi1 atoms chain along the *c* axis.

nied by strong Q1D characteristics, etc. Previous theoretical calculations have also argued that the valence band maximum of $Bi_{19}S_{27}I_3$ is mostly composed of S $3p$ states and the conduction band minimum mainly from Bi $6p$ states slightly mixed with S $3p$ orbitals [28]. In $Bi_{19}S_{27}(Br_{1-x}I_x)_3$ nanowires, despite lattice expansion by the chemical substitution of Br for I, it exhibits an unusual composition-independent band gap of ~ 0.82 eV, which was attributed to the very minor contributions of the halogens to the valence band maximum and conduction band minimum [28]. On the contrary, the composition of Bi and S may be an effective pathway to regulate electronic structures, but there are still no relevant experimental and theoretical reports, although a large amount of atomic disorder may weaken its functional parameters, such as the *ZT* values [1,13,26,27]. Another noteworthy issue is that the type of carrier also shows considerable dependence on the growth process of crystals, for example, the *n*- and *p*-type crystals can be obtained through the facile hydrothermal process followed by spark plasma sintering and chemical vapor transport method, respectively [26,27]. It is likely due to the formation of different impurity levels between semiconductor band gaps, and different doping level may affect the macroscopic transport characteristics of material. Another point is that strong anisotropy in Q1D-$Bi_{19}S_{27}I_3$ usually leads to the competition of low-energy excited states resulting from the instability of crystal structure and electronic states, which thus makes it a good candidate for exploring exotic phenomena [26,29,30], such as density wave (DW), SC, and Lifshitz transitions [31–34]. At present, it is thus worth exploring to grow high-quality Q1D-$Bi_{19}S_{27}I_3$ crystal, revealing its intrinsic physical properties and exploring potential functional properties.

High pressure is a clean probe method and can effectively modify the interactions of various degrees of freedom and electronic structures [35,36]. In $Bi_{19}S_{27}I_3$, it is expected to achieve semiconducting-metal transition or even possible superconducting states by adjusting the strength of chain spacing as well as interaction and lattice anisotropy through pressure [25–28]. In this paper, we grew high-quality $Bi_{19}S_{27}I_3$ by optimizing the chemical vapor transport method and studied its physical properties. At ambient pressure (AP),

$Bi_{19}S_{27}I_3$ is found to be a diamagnetic semiconductor with two thermal activation energies—a large one $E_{g1} \sim 0.81$ eV and a small one $E_{g2} \sim 0.36$ eV—a huge room-temperature Seebeck coefficient of -1000 μV/K, and significantly improved thermoelectric power factor ~ 2.2 μW cm^{-1} K^{-2}. Under hydrostatic pressures up to 11.5 GPa, $Bi_{19}S_{27}I_3$ undergoes a semiconducting-to-metal transition with a DW-like phase at intermediate pressures, and then the low-*T* resistivity shows an upturn below the characteristic temperature associated with possible Anderson weak localization. High-pressure synchrotron x-ray diffraction confirms that there is no structural transition for $P < 12.05$ GPa at room temperature. Our results are valuable to explore thermoelectric functional properties in low-dimensional materials.

II. EXPERIMENTAL METHODS

Single-crystal $Bi_{19}S_{27}I_3$ was grown by the chemical vapor transport method using I_2 as a transport agent. First, high-purity Bi and S powder (99.999%) with stochiometric ratio and excess I_2 (99.99%) were weighted, mixed, and placed into a silicon tube; the tube was sealed under $\frac{1}{3}$ atmospheric pressure argon gas and then heated in a two-zone furnace. During this process, the temperatures of heating and growth zones were set as 650 and 600°, respectively. After the reaction held for 15 d, black shiny crystals with maximum length of 2–3 mm were synthesized. Powder x-ray diffraction (XRD) at room temperature was performed by a Huber G670-V42833-3 diffractometer (Cu $K\alpha$, $\lambda = 1.5406$ Å). The Rietveld refinement of XRD patterns by FULLPROF software shows good fits ($\chi^2 \sim 1.20$, $R_p \sim 1.15$, and $R_{wp} \sim 2.33$), and all the peaks can be well indexed by a hexagonal phase with space group: $P63/m$, No. 176, as displayed in Fig. 1 [26,27]. A high-resolution transmission electron microscope (HRTEM) was adopted to resolve the atomic lattice images and the Fourier transform spectrum of $Bi_{19}S_{27}I_3$ [27]. All these characteristics consistently indicate high-quality $Bi_{19}S_{27}I_3$ [25–28]. At AP, electrical transport $\rho(T)$, the Seebeck coefficient $S(T)$, and Hall conductivity were measured in a Quantum Design Physical Property Measurement System (PPMS-9T) ($0 \leqslant H \leqslant 9.0$ T, $1.8 \leqslant T \leqslant 400$ K). The measure current is parallel to the *c* axis of $Bi_{19}S_{27}I_3$ and the field in the *ab* plane. For $\rho(T)$, a standard four-probe method was used with four parallel electrodes and intermediate electrodes for measuring voltage. For Hall conductivity measurements, different configurations of the contacts are used. The magnetoresistance (MR) and Hall voltage with the same accuracy and four contacts need a pair of misaligned voltage contacts on the sides of the crystals, perpendicular to both current and magnetic field (-8 to 8 T). Then symmetrization (antisymmetrization) of the measured voltage gives the MR (Hall) signal. Magnetic susceptibility was also measured with the applied magnetic field of 0.1 T parallel to the *c* axis on the Quantum Design Magnetic Property Measurement System ($0 \leqslant H \leqslant 9.0$ T, $1.8 \leqslant T \leqslant 300$ K).

A palm-type cubic anvil cell (CAC) was employed to measure $\rho(T)$ under hydrostatic pressures up to 11.5 GPa [37–39]. In CAC, high-density MgO cubes with enclosed Teflon in the center is used as the gasket. The triaxial symmetrical compression and the liquid glycerol as the pressure transmitting
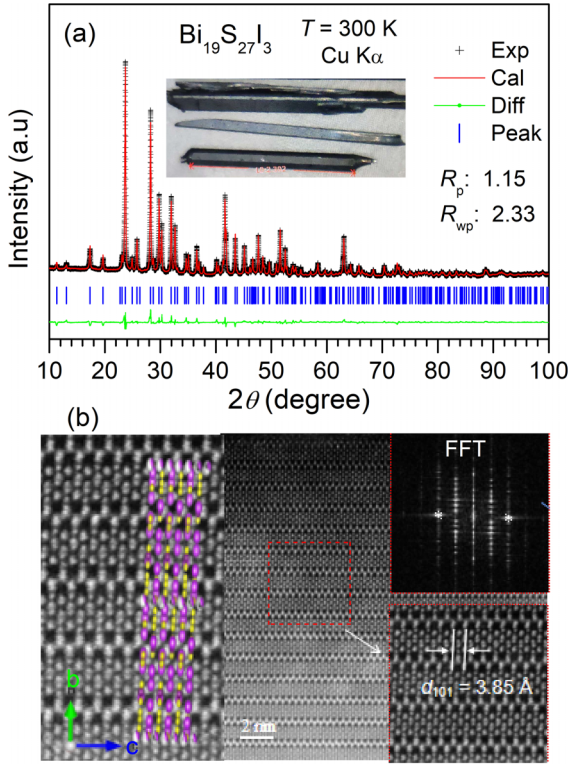
FIG. 2. (a) Powder x-ray diffraction at room temperature of the grounded single crystal and the Rietveld refinement using FULLPROF software. Inset: Images of grown $Bi_{19}S_{27}I_3$ single crystal. (b) High-resolution transmission electron microscope images and Fourier transform spectrum of single crystal $Bi_{19}S_{27}I_3$. The crystal plane [101] was calculated to be 3.85 Å after performing the inverse fast Fourier transform (FFT).

FIG. 3. (a) $\rho(T)$ of $Bi_{19}S_{27}I_3$ at AP. There is a weak metallic-semiconducting phase transition near the T_{M-I} (or T_1)≈ 260 K and two consecutive increasing behavior in resistivity around anomalous temperatures as $T_2 \approx 172$ K and $T_3 \approx 110$ K. Inset shows the enlargement of $\rho(T)$ data near T_{M-I} (one the left), the $\ln\rho$ vs $1000/T$ plot, and the fitting by a thermal activation model $\rho \sim \exp(E_g/k_B T)$ (on the right), which gives the thermal activation energies. (b) Temperature dependence of carrier concentration $n(T)$ and Hall coefficient; the dashed lines indicate the changing trend. Field-dependence of (c) Hall resistivity $\rho_{xy}(H)$ and (d) magnetoresistance (MR) with the fields up to 8.0 T under various temperatures, respectively.

medium (PTM) ensure a good hydrostatic environment [37]. The inside pressure was determined by measuring structural transitions of bismuth and tin at room temperature and superconducting transition of Pb at low temperatures. Under pressure, $\rho(T)$ was measured by the standard four-probe method with the current parallel to the c axis. All the experiments were performed in a ^{4}He refrigerated cryostat equipped with a superconducting magnet system ($4 \leqslant T \leqslant 300$ K). High-pressure synchrotron x-ray diffraction (HP-SXRD) at room temperature was measured in a diamond anvil pressure cell (DAC) at the beamline of the Synchrotron Radiation Station at Beijing Synchrotron Radiation Facility (BSRF). A rhenium gasket was preindented to $\sim 33 \,\mu$m and then a 100-μm-diameter hole was drilled in the center using a laser drilling system. The sample was grounded and mixed with the PTM before being placed into the pores of the DAC. The pressure in the DAC was determined by the ruby fluorescence method, and a Mar345 image plate was used to record the diffraction patterns. In this paper, DIOPTAS and GSAS programs were employed for image integration and Rietveld refinement of XRD patterns, respectively.

III. RESULTS AND DISCUSSIONS

We first characterized crystal structure and physical properties of single-crystal $Bi_{19}S_{27}I_3$ at AP. Figure 2(a) shows

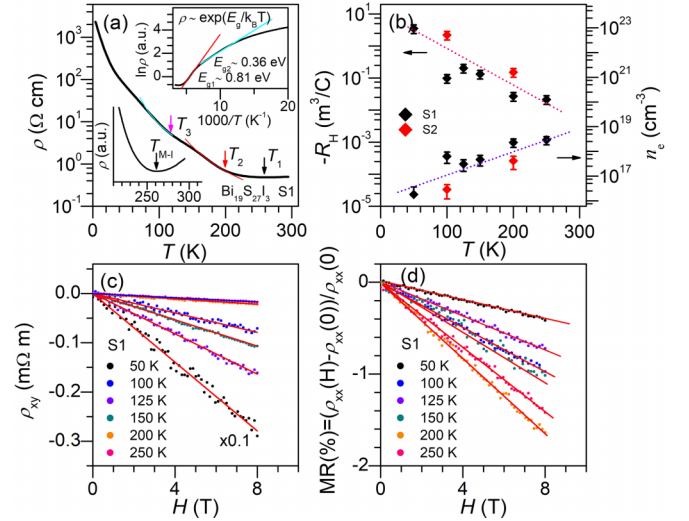the room-temperature XRD pattern and its good-fit Rietveld refinement. We found that the XRD pattern can be well indexed to a single hexagonal phase (space group: $P6_3/m$, No. 176) with lattice parameters of $a = b = 15.6203(6)$ Å and $c = 4.0211(4)$ Å, respectively. We noted that the estimated parameters are close to the reported values [25–27]. In Fig. 2(b), the HRTEM presents that all atoms have well-defined periodical arrangement; after performing the inverse fast Fourier transform (FFT), the distance d_{101} of the crystal plane [101] was ~ 3.85 Å, consistent with the above analysis [27]. Therefore, our results consistently confirm the high-quality hexagonal phase of $Bi_{19}S_{27}I_3$.

Figure 3 presents the temperature dependence of electrical transport $\rho(T)$ for $Bi_{19}S_{27}I_3$ at AP. It exhibits a weak metallic-semiconducting phase transition near the T_{M-I} (or T_1)≈ 260 K, as shown in the inset of Fig. 3(a), and then $\rho(T)$ increases rapidly by three orders of magnitude on cooling down to 2 K. However, there are two consecutive increasing behaviors with reducing the temperature, indicating that $Bi_{19}S_{27}I_3$ may have two semiconducting energy gaps at AP. To characterize them, we defined these anomalous temperatures as $T_2 \approx 172$ K and $T_3 \approx 110$ K, respectively. Accordingly, as displayed in Fig. 3(a), $\rho(T)$ is described by a thermal activation model $\rho \sim \exp(E_g/k_B T)$, where E_g and k_B represent the thermal activation energy and the Boltzmann constant, respectively. In Fig. 3(a) and its inset, the fitting results are in both $\ln\rho$-T and $\ln\rho$-$1000/T$ plots with the selections of two temperature ranges (140–220 and 70–120 K), which gives a large $E_{g1} \sim 0.81$ eV and a small $E_{g2} \sim 0.36$ eV comparable with

other reports [26–28]. Their differences might be attributed to the Q1D-crystal structure of the material with different levels of Bi vacancies and disorders along the Bi1 chain. It indicates that the sample quality may have significant impact on electronic structures. At room temperature, the resistivity is nearly three orders smaller in magnitude than those of other reports [26,27]. Although both E_{1g} and E_{2g} remain unchanged, there may be some additional electron doping or new impurity energy levels affecting the resistivity of semiconducting materials [40–42]. For clarify, we measured Hall resistivity $\rho_{xy}(H)$ of two $Bi_{19}S_{27}I_3$ crystals at temperatures (S1: 50, 100, 125, 150, 200, and 250 K and S2: 100 and 200 K) in Fig. 1S in the Supplemental Material [43]. Using the data, temperature dependence of $\rho_{xy}(H)$ and MR were derived in Figs. 3(c) and 3(d). For each temperature, $\rho_{xy}(H)$ exhibits an approximate linear relationship with the field. Using a single-band model, Hall coefficient $-R_H$ ($= 1/n_e e \sim 10^{-2}-10^1$ m^3/C) and carrier concentration n_e ($\sim 10^{17}-10^{19}$ cm^{-3}) were obtained in Fig. 3(b). The average concentration is greater than the ones of other intrinsic semiconductor [41,42], indicating high electron doping and the uniqueness of $Bi_{19}S_{27}I_3$. The dominant carrier type is n type between 50 and 300 K in $Bi_{19}S_{27}I_3$, different from the p type of $Bi_{19}S_{27}I_3$ with an indirect gap of 0.73 eV and a direct gap of 1.08 eV [27]. In Fig. 3(d), the MR shows nearly linear field dependence and is $< 2\%$ at 8.0 T for each temperature, which is attributed to the Lorentz scattering effect of electrons.

In Fig. 4(a), the temperature dependence of susceptibility of $Bi_{19}S_{27}I_3$ was measured at a magnetic field of 0.1 T, and it exhibits weak diamagnetism over the investigated temperature range of 2–300 K. At lower temperatures, $\chi(T)(=M/H)$ shows a slight upturn, which may result from small magnetic impurities. For clarity, low-T $\chi(T)$ ($=M/H$) was analyzed by the modified Curie-Weiss (CW) law $\chi(T) = \chi_A + C/(T - \theta_c)$, where χ_A, C, and θ_c represent the diamagnetic susceptibility, the effective moment, and the CW temperature, respectively. Here, we should note that χ_A can be seen as a sum of orbital and Landau diamagnetism, Pauli paramagnetism, etc. In the narrow low-temperature region, the first two are essentially unchanged, and thus, the $C/(T - \theta_c)$ term mainly contributes to the CW behavior. The fitting gives the following parameters: $\chi_A \sim -3.195 \times 10^{-7}$ emu/g Oe, $C \sim 2.023 \times 10^{-7}$ emu/g Oe, and $\theta = 3.89$ K, respectively. The negative χ_0 and positive θ indicate the diamagnetic state and weak ferromagnetic interaction, respectively. These two seemingly contradictory results precisely reflect that they may come from different magnetic sources. However, the absence of possible magnetic elements in $Bi_{19}S_{27}I_3$ reveals possible unknown trace ferromagnetic impurities and that it may enhance electron scatterings without affecting its semiconductor ground state. In Fig. 4(b), the temperature-dependent Seebeck coefficient $S(T)$ was plotted. We found that the S value shows linear temperature dependence and is negative in the whole temperature range, which indicates the dominant electron-type carriers, consistent with the results of Hall conductivity [26]. In the inset of Fig. 4(b) and Fig. 2S in the Supplemental Material [43], we also compared the temperature dependence of $S(T)$, $S(T)/T$, and $dS(T)/dT$. Although the overall dependence of $S(T)$ is linear, the metal-semiconducting phase transition (T_1) and the other
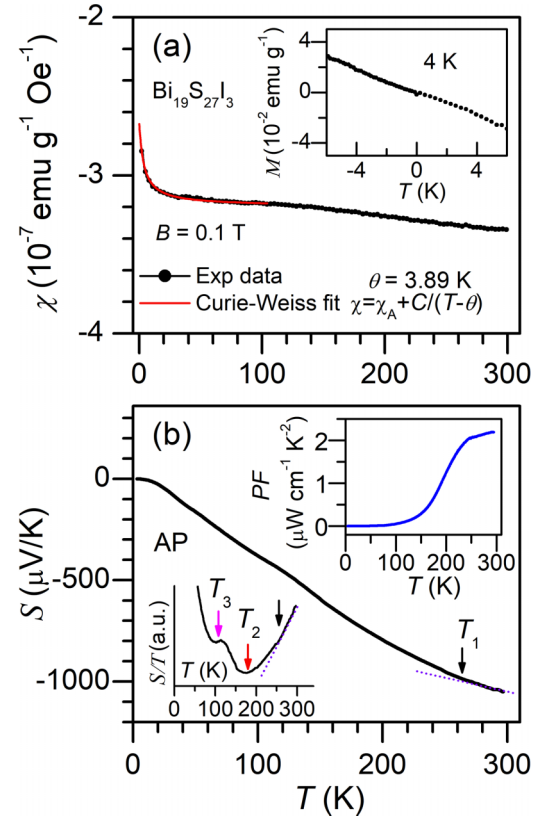

FIG. 4. (a) Magnetic susceptibility $\chi(T)$ ($=M/H$) under a magnetic field of 0.1 T at AP. Low-T $\chi(T)$ was analyzed by the Curie-Weiss (CW) law $\chi(T) = \chi_A + C/(T - \theta_c)$, where χ_A, C, and θ_c represent the sum of orbital and Landau diamagnetism, Pauli paramagnetism, etc.; the effective moment; and the Curie-Weiss temperature, respectively. (b) Seebeck coefficient $S(T)$; the inset shows the temperature dependence of power factor $PF(T)$. The arrows indicate the characteristic temperatures (T_1, T_2, and T_3).

two characteristic temperatures T_2 and T_3 from the electrical resistivity can be observed in both $S(T)/T$ and $dS(T)/dT$. More interestingly, the amplitude of S reaches a maximum of 1000 µV/K at 300 K [26,27]. Using the above S and ρ, we get the power factor $PF = S^2\sigma$, where σ ($\sigma = 1/\rho$) represents the electrical conductivity of the material [43]. For single-crystal $Bi_{19}S_{27}I_3$ at AP, the PF reaches 2.2 µW cm^{-1} K^{-2} at 300 K in the inset of Fig. 4(b), nearly one order of magnitude larger than those of typical thermoelectric materials [44–51] and the $Bi_{19}S_{27}I_3$ grown by the facile hydrothermal process [26]. The PF $\sim$ 2.2 µW cm^{-1} K^{-2} at 300 K is comparable with some classical thermoelectric materials such as SnSe, $Bi_2(S, Se, Te)_3$ (see Table I) [46–51]. As mentioned above, its enhancement can be attributed to the reduced resistivity resulting from impurity doping. However, in previous reports [26,27], the resistivity of $Bi_{19}S_{27}I_3$ is measured by a probable two-contact methods used for nanomicrorod samples. It suggests that the origin of higher conductivity at room temperature is not only related to the sample quality or the doping level but also attributed to the four-probe method. Another issue worth considering is that $Bi_{19}S_{27}I_3$ is a semiconductor dominated by n-type carriers, and different mobilities may also be an important reason.

TABLE I. The typical values of power factor at room temperature for several classical thermoelectric materials such as SnSe, Bi_2Te_3, and Bi_2Se_3 are compared. These results indicate $Bi_{19}S_{27}I_3$ may be a candidate thermoelectric material.

Material	PF ($\mu W\,cm^{-1}\,K^{-2}$) at 300 K	Direction	Reference
SnSe	2–3	//b and //c	[45,46]
Bi_2Se_3	~2	Polycrystal	[47]
Bi_2Se_3	~8	Nanostructure	[48]
Bi_2Te_3	~3	Polycrystal	[49]
Bi_2S_3	0.53	Polycrystal	[50]
$Bi_{19}S_{27}I_3$	~2.2	//c	This paper

Figure 5 displays the temperature dependence of $\rho(T)$ for $Bi_{19}S_{27}I_3$ under pressure in CAC up to 11.5 GPa. With increasing pressure, both $\rho(10\,K)$ and $\rho(300\,K)$ decrease rapidly by nearly six and three orders of magnitude compared with that at AP, respectively. In Fig. 5(a), we found that the value of T_{M-I} (T_1) decreases from 260 K at AP to 200 K at 3.25 GPa and disappears completely ~ 4.25 GPa, which confirms a pressure-induced semiconducting-to-metal phase transition. Accompanying this, a DW-like phase transition emerges near T_2 with a reversible resistivity jump in the range of 2.5–4.25 GPa [52]. To get more insight on the DW-like transition, $\rho(T)$ was measured for 3.5 and 4.25 GPa on warming and cooling processes in Fig. 6, respectively. The $\rho(T)'$ curve coincide perfectly without any thermal hysteresis, ruling out the possibility of structural transition. With further increasing pressure, low-T resistivity starts to undergo the crossover from a Fermi metal to an upturn behavior below a characteristic temperature T_4. At first, for 4.5 and 6.0 GPa, the minimum or dip at low temperatures in resistivity is spread over a T region, as shown in Fig. 3S in the Supplemental Material [43], which may imply that the DW-like phase transition is not
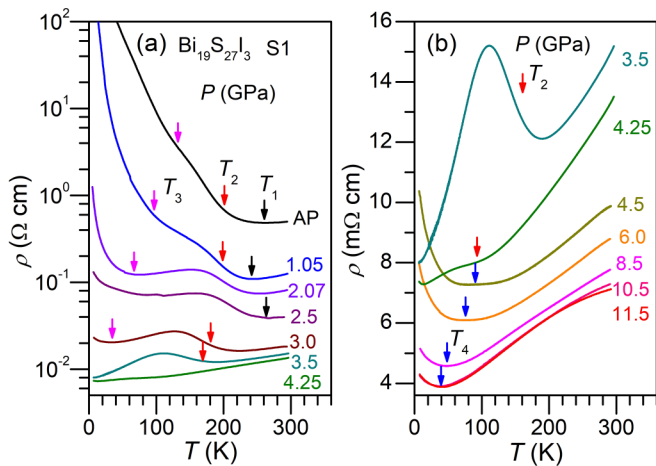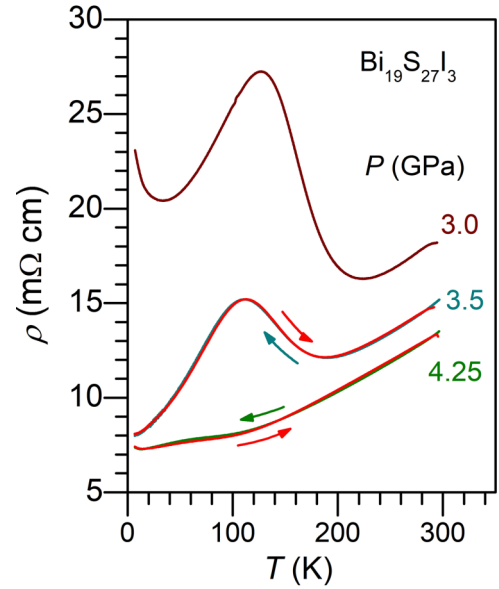

FIG. 6. $\rho(T)$ under pressures (3.5 and 4.25 GPa) on warming and cooling processes, respectively.

suddenly disappearing, possibly forming short-range DW. As the pressure increases, the dip at low temperatures becomes more pronounced, ultimately resulting in Kondo-like behavior (e.g., $\rho(T) \sim -lnT$) [43,53]. At the same time, T_4 reduces monotonically from 81 K at 4.5 GPa to 37 K at 11.5 GPa. Such a low-temperature upturn mainly reflects more electron scatterings from phonon or atomic disorders. To further confirm the hypothesis, we fitted the temperature dependence of resistivity at 4.5–11.5 GPa by the empirical formula $\rho(T) = A_0 - B_0 ln(T/T_5)$ in Fig. 7(a). As the pressure increases, both the A_0 and B_0 values monotonically decrease and tend to saturate at $P > 10$ GPa. Interestingly, the derived T_5 perfectly matches T_4 determined from $\rho(T)$ data in Fig. 5(b), demonstrating the reliability of the previous data. However, we also found, in Fig. 7(a), the resistivity is basically linear with the
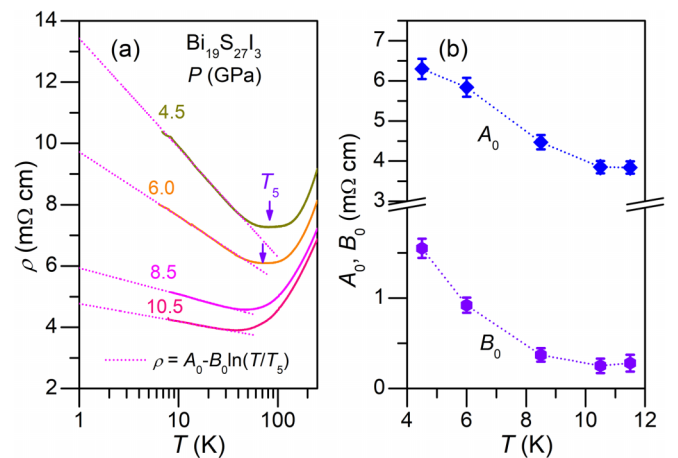

FIG. 5. $\rho(T)$ under hydrostatic pressures: (a) 0–4.25 GPa; the black, red, and magenta arrows represent the metal-insulator transition T_1, the characteristic temperature T_2 for the density-wave (DW)-like transition, and low-temperature anomalous temperatures T_3, respectively. (b) 3.5–11.5 GPa; the blue arrow refers to the temperature T_4 for the low-temperature upturn in resistivity.

FIG. 7. (a) Temperature dependence of resistivity at 4.5–11.5 GPa and its low-temperature data fitting by the empirical formula $\rho(T) = A_0 - B_0 ln(T/T_5)$. (b) The evolution of parameters A_0 and B_0 as a function of pressure. We note that the derived T_5 perfectly matches the T_4 determined from $\rho(T)$ data in Fig. 5(b).
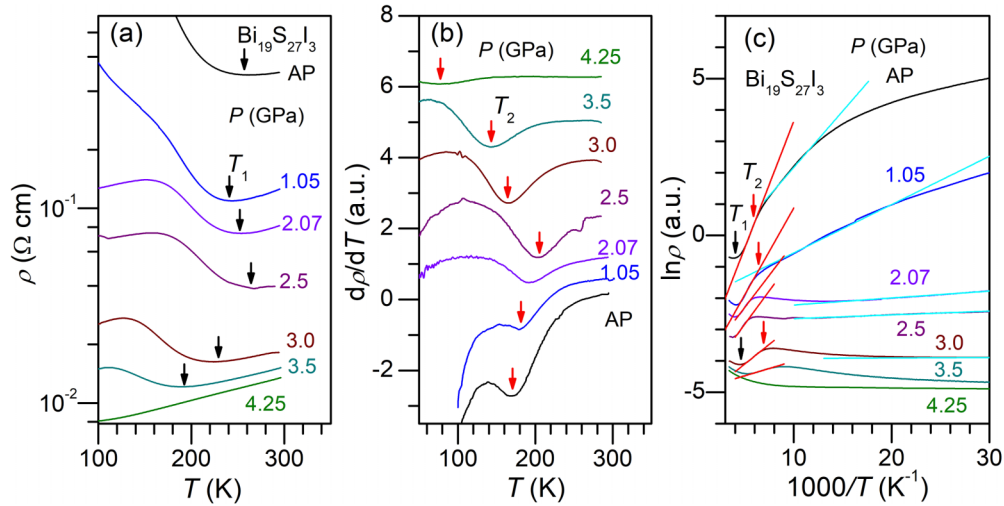
FIG. 8. (a) High-temperature $\rho(T)$ under various pressures and (b) its derivative $d\rho/dT(T)$. (c) $\ln\rho$ vs $1000/T$ plot and the fitting results by a thermal activation model under various pressures up to 4.25 GPa. The black and red arrows in (a) and (b) represent T_1 and T_2, respectively.

logarithmic temperature but not saturated at low temperatures, which may basically rule out the Kondo-like state with an usually saturated resistivity at the lowest temperature. Therefore, we are more inclined to believe that it is the enhanced scattering effect induced by Anderson weak localization. Thus, our analysis supports the enhanced electron scattering caused by impurities after pressure-induced metallization at $P > 3.5$ GPa.

To get the evolution of all the characteristic temperatures with pressure, we compared $\rho(T)$ and the derivative $d\rho/dT(T)$ in Figs. 5(a), 5(b), 8(a), and 8(b). We found that both the T_1 and T_2 values exhibit the same nonmonotonic pressure dependence: first enhancing and then reducing with increasing pressure. Here, T_3 monotonically decreases to nearly zero at $P \sim 3.0$ GPa. Both thermal activation energies E_{g1} and E_{g2} are calculated by the ρ-$1000/T$ plot displayed in Figs. 8(c). Based on the resistivity data, we drew a temperature-pressure phase diagram of $Bi_{19}S_{27}I_3$, shown in Figs. 9(a), where the colors represent the changes of electrical resistivity, the pressure-driven semiconductor-metal transition, and the increase of low-temperature resistivity under pressures. The pressure dependences of the characteristic parameters T_1, T_2, T_3, T_4, T_5, $\rho(300 \text{ K})$, $\rho(10 \text{ K})$, E_{1g}, and E_{2g} are summarized in Figs. 9(b)–9(d). Both T_1 and T_2 decrease with increasing pressure and disappear completely at 4.25 GPa. Accompanying this, both thermal activation energies E_{g1} and E_{g2} reduce continuously to nearly zero, evidencing the semiconducting-to-metallic transition. With further increasing pressure up to 11.5 GPa, the T_4 and T_5 values reduce in succession to 38 K and then completely disappear at about 20 GPa from the linear extrapolation of temperature-pressure relation.

To clarify the pressure effect on the crystal structure of $Bi_{19}S_{27}I_3$ crystal, high-pressure x-ray diffraction (HPXRD) at room temperature was performed up to 12.05 GPa, as in Fig. 10(a). In our pressure range, there is no clear splitting and/or emergence of new diffraction peaks, and thus no pressure-induced structural transition is concluded according to the refinement of XRD patterns. The pressure dependence of lattice parameters (a, c, V) and the relative shrinkage (a/a_0,

c/c_0, V/V_0) are obtained by Rietveld refinement and plotted in Figs. 10(b) and 10(c). The lattice parameters (a, c, V) contract monotonically with pressure and reduce by ~ 3.5, 5.0, and 6.5% at 12.05 GPa compared with those at AP, which indicates an anisotropic contraction under pressure. The relative shrinkage of c/a shows a slightly increase from 0.257 at AP to 0.261 at 12.05 GPa. In this regard, the pressure-induced semiconducting-to-metallic transition in $Bi_{19}S_{27}I_3$ can be attributed to the enhanced hybridization of different electron orbitals under pressure [28] and needs further in-depth research. However, our present preliminary results only confirm the absence of structural phase transition at room temperature. Considering the Q1D-$Bi_{19}S_{27}I_3$ crystal, it seems unlikely that structural phase transitions will only occur at low tem-
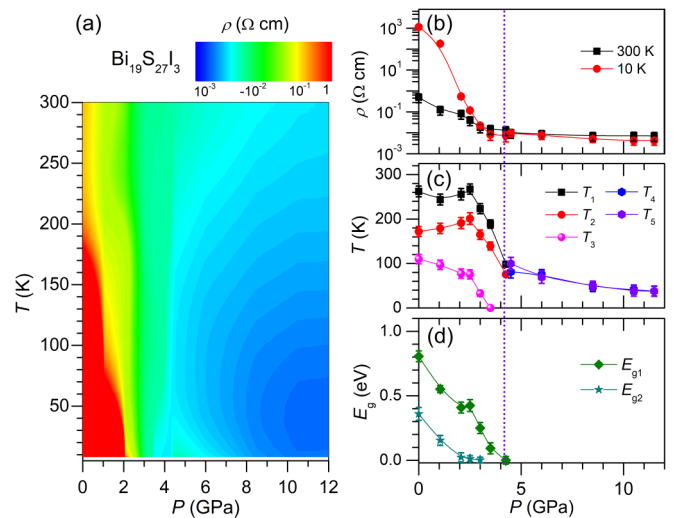

FIG. 9. (a) The temperature-pressure phase diagram of $Bi_{19}S_{27}I_3$ where the colors represent the changes of electrical resistivity. The pressure dependence of the characteristic parameters: (b) $\rho(300 \text{ K})$ and $\rho(10 \text{ K})$; (c) T_1, T_2, T_3, T_4, and T_5; and (d) thermal activation energies E_{g1} and E_{g2} determined by the thermal activation model. The lines across the data indicate the changing trend.
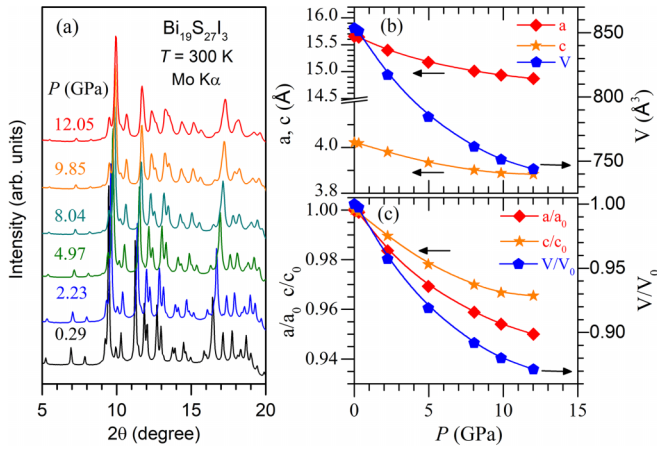
FIG. 10. (a) Synchrotron x-ray diffraction patterns of $Bi_{19}S_{27}I_3$ at room temperature under various pressures up to 12.05 GPa. (b) The pressure dependence of lattice parameters (a, c, V). The relative shrinkage of c/a shows a slightly increase from 0.257 at AP to 0.261 at 12.05 GPa. (c) The pressure dependence of the relative lattice parameters (a/a_0, c/c_0, V/V_0). Here, the a_0, c_0, and V_0 are the lattice parameters at AP.

peratures, often maintaining them beyond room temperature if concurring. Another noteworthy point is that, under pressure, the electrical transport data undergo continuous changes without significant overlap, but most of all, structural phase transitions are often accompanied by sharp changes in electronic states, leading to jumps in electrical transport. The upward trend of resistance at high pressure and low temperature is more likely to be attributed to the strengthening effect of Anderson weak localization. Nonetheless, there may also be another mechanism, for example, the enhanced electron-phonon coupling leads to the upward trend of resistance at high pressure and low temperature. We may know that strong electron-phonon coupling is an important CDW mechanism, even for Q1D-CDW transitions usually from Fermi surface nesting [54,55]. Although our inference and hypothesis description of the experimental data are reasonable, more future experiments are needed to verify the existence or absence of low-temperature and high-pressure phase transitions as well as to reveal the origin of DW-like phase transition in $Bi_{19}S_{27}I_3$ crystals.

Finally, we discuss several important issues. The first one is the mechanism of pressure-induced semiconducting-metallic phase transition of $Bi_{19}S_{27}I_3$ near a critical pressure of 3.0–4.25 GPa and the following crossover from Fermi metal and low-temperature upturn in resistivity. Considering the absence of structural phase transition, our density functional theory calculation was carried out on the assumption that the Bi1 site has an occupancy ration of $\sim \frac{1}{6}$, and the results are shown in Fig. 4S in the Supplemental Material [43]. However, we found that the electron band dominated by Bi 6p and S 3p electron orbitals did not open an energy gap, which greatly contradicts with the AP data [28]. This indirectly indicates that Bi1 should be partially ordered and have many vacancies, which determines the complex electronic structure of $Bi_{19}S_{27}I_3$ [28]. Indeed, studies on the physical properties at AP have revealed that the presence of large vacancies and impurity energy levels in $Bi_{19}S_{27}I_3$ may introduce carrier doping and result in much

enhancement of conductivity and PF values. To answer these questions more accurately, in the future, larger supercells may be required to delineate the Bi1 atomic arrangements and electronic structures of $Bi_{19}S_{27}I_3$.

Secondly, the emergent DW-like transition at intermediate pressures of 3.0–4.0 GPa is interesting especially in Q1D-$Bi_{19}S_{27}I_3$. We note that the observed upturn behavior of resistivity under pressure is very similar to some other Q1D materials presenting a CDW transition, such as $NbSe_3$, $HfTe_3$, and CuTe [54,56,57]. However, the specific characteristics and origin of DW-like transition in Q1D-$Bi_{19}S_{27}I_3$ are difficult to explore. Based on the above high-pressure electrical transport and smooth pressure dependence of the lattice parameters at room temperature, it is possible to exclude the structural transition at low temperatures and the case of Q1D-DW-like transition in $Bi_{19}S_{27}I_3$, which often accompanies the characteristics of first-order phase transition such as evident thermal hysteresis on cooling and warming processes. Our results indirectly demonstrate that DW-like transition is not simply a vibration mode along the c axis, although it is difficult to determine the Q1D or quasi-two-dimensional DW-like phase transition in $Bi_{19}S_{27}I_3$, which is still an open question that requires further experimental and theoretical evidence, e.g., low-temperature and high-pressure XRD or neutron diffraction. In addition, the collapse of DW-like transition by pressure does not lead to any signature of SC, which may indicate weak electron-phonon coupling and/or strong competition between SC and some other undetected excited state under pressure.

The last one is the origin of the crossover from Fermi metal to a low-temperature upturn behavior at $P > 4.5$ GPa. Usually, the strong scattering of conductive electrons by local magnetic moments is the main physical mechanism of Kondo-like behavior; however, our studies have shown that there is no magnetic moment in $Bi_{19}S_{27}I_3$, indicating that the emergent Kondo-like behavior is incomprehensible. Another possibility is that there is some small energy gap in the partial Fermi surface with an enhancement of electron scatterings under pressure and/or the Anderson weak localization effect caused by disorder. This speculation coincides with our experiment: The upturn in low-temperature resistivity is mainly attributed to Anderson weak localization rather than the Kondo effect, which is mainly due to the absence of a magnetic moment in $Bi_{19}S_{27}I_3$ and the lack of low-temperature saturation resistivity frequently used to prove the Kondo effect. Here, we should note that physical pressure does not introduce impurities, and the upturn of resistivity is mainly accompanied by a pressure-induced metallization and an increasing carrier concentration which causes the strong scatterings. At present, the physical mechanism involved in this issue requires further theoretical calculations and experimental explorations, such as the occupation of Bi1 atoms in $Bi_{19}S_{27}I_3$.

IV. CONCLUSIONS

In summary, we grew high-quality Q1D-$Bi_{19}S_{27}I_3$ crystal and characterized its electrical resistivity, magnetic properties, Seebeck coefficient, Hall coefficient, and hydrostatic pressure effect. We found that the $Bi_{19}S_{27}I_3$ crystal can reach 2–3 mm by optimizing the chemical vapor transport

method and is an *n*-type diamagnetic semiconductor with two thermal activation energies—a large one $E_{g1} \sim 0.81$ eV and a small one $E_{g2} \sim 0.36$ eV—and an improved thermoelectric power factor $\sim 2.2\,\mu\text{W}\,\text{cm}^{-1}\,\text{K}^{-2}$ owing to the much enhanced electrical conductivity, which is comparable with classical thermoelectric materials. Under pressure, a crossover from semiconducting to metallic state with an evident completely reversible DW-like transition is observed at $P \sim 4.25$ GPa, and one more low-temperature upturn behavior emerges up to 11.5 GPa. HPXRD was performed, and the analysis suggests that there is no pressure-induced structural transition up to 12 GPa at room temperature.

ACKNOWLEDGMENTS

[1] A. Parida, S. Senapati, and R. Naik, Recent developments on Bi-based oxychalcogenide materials with thermoelectric and optoelectronic applications: An overview, Mater. Today Chem. **26**, 101149 (2022).

[2] C. Barreteau, L. Pan, E. Amzallag, L. D. Zhao, D. Berardan, and N. Dragoe, Layered oxychalcogenide in the Bi-Cu-O-Se system as good thermoelectric materials, Semicond. Sci. Technol. **29**, 064001 (2014).

[3] A. M. Eufrasio, I. Pegg, A. Lafle, W. Wong-Ng, Q. Z. Huang, and B. Dutta, Metal-insulator transition in doped barium plumbates, Electron. Mater. **2**, 428 (2021).

[4] A. W. Sleight, J. L. Gillson, and P. E. Bierstedt, High-temperature superconductivity in $BaPb_{1-x}Bi_xO_3$ system, Solid State Commun. **17**, 27 (1975).

[5] C. Parra, F. C. Niestemski, A. W. Contryman, P. Giraldo-Gallo, T. H. Geballe, I. R. Fisher, and H. C. Manoharan, Signatures of two-dimensional superconductivity emerging within a three-dimensional host superconductor, Proc. Natl Acad. Sci. U.S.A. **118**, 16e2017810118 (2021).

[6] M. Kim, G. M. McNally, H. Kim, M. Oudah, A. S. Gibbs, P. Manuel, R. J. Green, R. Sutarto, T. Takayama, A. Yaresko *et al.*, Superconductivity in (Ba, K)SbO$_3$, Nat. Mater. **21**, 627 (2022).

[7] Y. S. Hor, A. J. Williams, J. G. Checkelsky, P. Roushan, J. Seo, Q. Xu, H. W. Zandbergen, A. Yazdani, N. P. Ong, and R. J. Cava, Superconductivity in $Cu_xBi_2Se_3$ and its implications for pairing in the undoped topological insulator, Phys. Rev. Lett. **104**, 057001 (2010).

[8] K. Kirshenbaum, P. S. Syers, A. P. Hope, N. P. Butch, J. R. Jeffries, S. T. Weir, J. J. Hamlin, M. B. Maple, Y. K. Vohra, and J. Paglione, Pressure-induced unconventional superconducting phase in the topological insulator Bi_2Se_3, Phys. Rev. Lett. **111**, 087001 (2013).

[9] T. V. Bay, T. Naka, Y. K. Huang, H. Luigjes, M. S. Golden, and A. de Visser, Superconductivity in the doped topological insulator $Cu_xBi_2Se_3$ under high pressure, Phys. Rev. Lett. **108**, 057001 (2012).

[10] R. Tao, Y.-J. Yan, X. Liu, Z.-W. Wang, Y. Ando, Q.-H. Wang, T. Zhang, and D.-L. Feng, Direct visualization of the nematic superconductivity in $Cu_xBi_2Se_3$, Phys. Rev. X **8**, 041024 (2018).

[11] G. Catalan and J. F. Scott, Physics and applications of bismuth ferrite, Adv. Mater. **21**, 2463 (2009).

[12] F. Matsukura, Y. Tokura, and H. Ohno, Control of magnetism by electric fields, Nat. Nanotechnol. **10**, 209 (2015).

[13] Y. Pan and J. F. Li, Thermoelectric performance enhancement in *n*-type $Bi_2(TeSe)_3$ alloys owing to nanoscale inhomogeneity combined with a spark plasma-textured microstructure, NPG Asia Mater. **8**, 275 (2016).

[14] B. Poudel, Q. Hao, Y. Ma, Y. Lan, A. Minnich, B. Yu, X. Yan, D. Wang, A. Muto, D. Vashaee *et al.*, High-thermoelectric performance of nanostructured bismuth antimony telluride bulk alloys, Science **320**, 634 (2008).

[15] D. Parker and D. J. Singh, Potential thermoelectric performance from optimization of hole-doped Bi_2Se_3, Phys. Rev. X **1**, 021005 (2011).

[16] J. Shi, E. A. Rubinstein, W. W. Li, J. Y. Zhang, Y. Yang, T.-L. Lee, C. D. Qin, P. Yan, J. L. MacManus-Driscoll, D. O. Scanlon *et al.*, Modulation of the Bi^{3+} $6s^2$ lone pair state in perovskites for high-mobility *p*-type oxide semiconductors, Adv. Sci. **9**, 2104141 (2022).

[17] L. E. Díaz-Sánchez, A. H. Romero, and X. Gonze, Phonon band structure and interatomic force constants for bismuth: Crucial role of spin-orbit interaction, Phys. Rev. B **76**, 104302 (2007).

[18] T. Hirahara, T. Nagao, I. Matsuda, G. Bihlmayer, E. V. Chulkov, Yu. M. Koroteev, P. M. Echenique, M. Saito, and S. Hasegawa, Role of spin-orbit coupling and hybridization effects in the electronic structure of ultrathin Bi films, Phys. Rev. Lett. **97**, 146803 (2006).

[19] Y. F. Li, E. Y. Wang, X. Y. Zhu, and H. H. Wen, Pressure-induced superconductivity in Bi single crystals, Phys. Rev. B **95**, 024510 (2017).

[20] O. Degtyareva, M. I. MCMahon, and R. J. Nelmes, High-pressure structural studies of group-15 elements, High Pressure Res. **24**, 319 (2004).

[21] T. K. Kim, J. Wells, C. Kirkegaard, Z. Li, S. V. Hoffmann, J. E. Gayone, I. Fernandez-Torrente, P. Häberle, J. I. Pascual,

K. T. Moore *et al.*, Evidence against a charge density wave on Bi(111), Phys. Rev. B **72**, 085440 (2005).

[22] V. G. Orlov, G. S. Sergeev, and E. A. Kravchenko, Bismuth and antimony chalcogenides: Peculiarities of electron density distribution, unusual magnetic properties and superconductivity, J. Magn. Magn. Mater. **475**, 627 (2019).

[23] H. F. Zhai, W. H. Jiao, Y. L. Sun, J. L. Bao, H. Jiang, X. J. Yang, Z. T. Tang, Q. Tao, X. F. Xu, Y. K. Li *et al.*, Superconductivity, charge- or spin-density wave, and metal-nonmetal transition in $BaTi_2(Sb_{1-x}Bi_x)_2O$, Phys. Rev. B **87**, 100502(R) (2013).

[24] T. Yajima, K. Nakano, F. Takeiri, T. Ono, Y. Hosokoshi, Y. Matsushita, J. Heister, Y. Kobayashi, and H. Kageyama, Superconductivity in $BaTi_2Sb_2O$ with a d^1 square lattice, J. Phys. Soc. Jpn. **81**, 103706 (2012).

[25] G. Z. Shen, D. Chen, K. Tang, L. Y. Huang, and Y. T. Qian, Large-scale synthesis of $(Bi(Bi_2S_3)_9I_3)_{0.667}$ submicrometer needle-like crystals via a novel polyol route, J. Cryst. Growth **249**, 331 (2003).

[26] J. Guo, L. Chen, Y. Wu, J. T. Xu, D. H. Lu, J. Feng, and Z. H. Ge, Facile synthesis of *n*-type hexagonal $(Bi(Bi_2S_3)_9I_3)_{0.667}$ as a promising thermoelectric compound, Chem. Commun. **56**, 11839 (2020).

[27] C. H. Ho, Y. H. Chen, Y. K. Kuo, and C. W. Liu, The structure and opto-thermo electronic properties of a new $(Bi(Bi_2S_3)_9I_3)_{0.667}$ hexagonal nano-/micro-rod, Chem. Commun. **53**, 3741 (2017).

[28] Y. H. Wu, H. H. Pan, X. Zhou, M. R. Li, B. Zhou, C. Yang, W. H. Zhang, J. S. Jie, and C. Li, Shape and composition control of $Bi_{19}S_{27}(Br_{3-x}I_x)$ alloyed nanowires: The role of metal ions, Chem. Sci. **6**, 4615 (2015).

[29] P. Santini, G. Fáth, Z. Domański, and P. Erdős, Quantum fluctuations and anisotropy in quasi-one-dimensional antiferromagnets, Phys. Rev. B **56**, 5373 (1997).

[30] I. Boettcher and I. F. Herbut, Anisotropy induces non-Fermi-liquid behavior and nematic magnetic order in three-dimensional Luttinger semimetals, Phys. Rev. B **95**, 075149 (2017).

[31] S. J. Denholme, A. Yukawa, K. Tsumura, M. Nagao, R. Tamura, S. Watauchi, I. Tanaka, H. Takayanagi, and N. Miyakawa, Coexistence of superconductivity and charge-density wave in the quasi-one-dimensional material $HfTe_3$, Sci. Rep. **7**, 45217 (2017).

[32] Z. Y. Liu, J. Li, J. F. Zhang, J. Li, P. T. Yang, S. Zhang, G. F. Chen, Y. Uwatoko, H. X. Yang, Y. Sui *et al.*, Quasi-one-dimensional superconductivity in the pressurized charge-density-wave conductor $HfTe_3$, npj Quantum Mater. **6**, 90 (2021).

[33] P. Di Pietro, M. Mitrano, S. Caramazza, F. Capitani, S. Lupi, P. Postorino, F. Ripanti, B. Joseph, N. Ehlen, A. Grüneis *et al.*, Emergent Dirac carriers across a pressure-induced Lifshitz transition in black phosphorus, Phys. Rev. B **98**, 165111 (2018).

[34] Q. Li, Y. X. Wu, X. Fan, Y. J. Zhang, X. Y. Zhu, Z. Y. Zhu, Y. W. Li, and H. H. Wen, Superconductivity arising from pressure-induced emergence of a Fermi surface in the kagome-lattice chalcogenide $Rb_2Pd_3Se_4$, Phys. Rev. B **106**, 214501 (2022).

[35] H. G. Drickamer, The effect of high pressure on the electronic structure of solids, Solid State Phys. **17**, 1 (1965).

[36] S. Schilling, The use of high pressure in basic and materials science, J. Phys. Chem. Solids **59**, 553 (1998).

[37] N. Mori, H. Takahashi, and N. Takeshita, Low-temperature and high-pressure apparatus developed at ISSP, University of Tokyo, High Pressure Res. **24**, 225 (2004).

[38] J.-G. Cheng, K. Matsubayashi, S. Nagasaki, A. Hisada, T. Hirayama, M. Hedo, H. Kagi, and Y. Uwatoko, Integrated-fin gasket for palm cubic-anvil high pressure apparatus, Rev. Sci. Instrum. **85**, 093907 (2014).

[39] J.-G. Cheng, B. S. Wang, J. P. Sun, and Y. Uwatoko, Cubic anvil cell apparatus for high-pressure and low-temperature physical property measurements, Chin. Phys. B **27**, 077403 (2018).

[40] E. T. Jira, Temperature dependence of electrical resistivity of (III, Mn)V diluted magnetic semiconductors, in *New Advances in Semiconductors*, edited by A. A. Cavalheiro (IntechOpen, London, 2022).

[41] P. P. Altermatt, A. Schenk, F. Geelhaar, and G. Heiser, Reassessment of the intrinsic carrier density in crystalline silicon in view of band-gap narrowing, J. App. Phys. **93**, 1598 (2003).

[42] C. Kittel, *Introduction to Solid State Physics* (John Wiley and Sons, Singapore, 2018).

[43] See Supplemental Material at http://link.aps.org/supplemental/10.1103/PhysRevB.109.144107 for the electrical transport and initial density functional theory calculations of BiSI.

[44] P. F. P. Poudeu, J. D'Angelo, A. D. Downey, J. L. Short, T. P. Hogan, and M. G. Kanatzidis, High thermoelectric figure of merit and nanostructuring in bulk *p*-type $Na_{1-x}Pb_mSb_yTe_{m+2}$, Angew. Chem., Int. Ed. **45**, 3835 (2006).

[45] A. Soni, Z. Yanyuan, Y. Ligen, M. K. K. Aik, M. S. Dresselhaus, and Q. Xiong, Enhanced thermoelectric properties of solution grown $Bi_2Te_{3-x}Se_x$ nanoplatelet composites, Nano Lett. **12**, 1203 (2012).

[46] Y. S. Zhang, S. Q. Hao, L. D. Zhao, C. Wolverton, and Z. Zeng, Pressure induced thermoelectric enhancement in SnSe crystals, J. Mater. Chem. A **4**, 12073 (2016).

[47] L. D. Zhao, G. J. Tan, S. Q. Hao, J. Q. He, Y. L. Pei, H. Chi, H. Wang, S. K. Gong, H. B. Xu, V. Y. P. Dravid *et al.*, Ultrahigh power factor and thermoelectric performance in hole-doped single-crystal SnSe, Science **351**, 141 (2015).

[48] A. M. Adam, A. Elshafaie, A. El-Moez A Mohamed, P. Petkov, and E. M. M. Ibrahim, Thermoelectric properties of Te doped bulk Bi_2Se_3 system, Mater. Res. Express **5**, 035514 (2018).

[49] G. L. Sun, L. L. Li, X. Y. Qin, D. Li, T. H. Zou, H. X. Xin, B. J. Ren, J. Zhang, Y. Y. Li, and X. J. Li, Enhanced thermoelectric performance of nanostructured topological insulator Bi_2Se_3, Appl. Phys. Lett. **106**, 053102 (2015).

[50] M. Saleemi, M. S. Toprak, S. Li, M. Johnsson, and M. Muhamme, Synthesis, processing, and thermoelectric properties of bulk nanostructured bismuth telluride (Bi_2Te_3), J. Mater. Chem. **22**, 725 (2012).

[51] F. Xu, C. Xu, H. M. Chen, D. P. Wu, Z. Y. Gao, X. M. Ma, Q. Zhang, and K. Jiang, The synthesis of $Bi_2S_3/2D-Bi_2WO_6$ composite materials with enhanced photocatalytic activities, J. Alloys Compd. **780**, 634 (2019).

[52] C. N. Kuo, R. Y. Huang, Y. K. Kuo, and C. S. Lue, Transport and thermal behavior of the charge density wave phase transition in CuTe, Phys. Rev. B **102**, 155137 (2020).

[53] N. Emi, N. Kawamura, M. Mizumaki, T. Koyama, N. Ishimatsu, G. Pristáš, T. Kagayama, K. Shimizu, Y. Osanai, F. Iga *et al.*, Kondo-like behavior near the magnetic instability in SmB_6: Temperature and pressure dependences of the Sm valence, Phys. Rev. B **97**, 161116(R) (2018).

[54] S. Y. Wang, X. L. Chen, C. An, Y. Zhou, Y. H. Zhou, C. C. Gu, L. L. Zhang, X. P. Yang, and Z. R. Yang, Pressure-induced superconductivity in the quasi-one-dimensional charge density wave material CuTe, Phys. Rev. B **103**, 134518 (2021).

[55] M. Campetella, G. Marini, J. S. Zhou, and M. Calandra, Electron-phonon driven charge density wave in CuTe, Phys. Rev. B **108**, 024304 (2023).

[56] A. A. Balandin, F. Kargar, T. T. Salguero, and R. K. Lake, One-dimensional van der Waals quantum materials, Mater. Today **55**, 74 (2022).

[57] K. Fujiwara, S. Iwakiri, M. Watanabe, R. Nakamura, M. Yokoi, K. Kobayashi, and Y. Niimi, Charge density wave transitions in mechanically-exfoliated NbSe$_3$ devices, Jpn. J. Appl. Phys. **60**, 070904 (2021).